

## Chapter 2

### Synthesis and characterization of CSA doped PANi-Ta<sub>2</sub>O<sub>5</sub> nanocomposite

#### 2.1 Introduction: Synthesis process of conducting polymers

Conducting polymers (CPs) have been traditionally synthesized either by chemical oxidative polymerization or electrochemical oxidation of the corresponding monomers. Both the routes produce an insulating material that requires a subsequent doping process. The overall polymerization process is followed by coupling reaction that produces a chain of the charged monomer units.

##### 2.1.1 Electrochemical Polymerization

In case of electrochemical polymerization, one-step in-situ process takes place which deposits the CP nanomaterial onto the surface of the electrode as a layer for a sensor device. This film grows along the direction of the electric field to form regularly oriented nanostructure. Polymerization takes place in a strong aqueous acidic condition of the electrolyte using radical polymerization. This process forms anilinium radical cation by aniline oxidation on the electrode [83].

The morphology and the film thickness of the deposited polymer can well be controlled by varying different electrochemical polymerization parameters such as the applied potential, polymerization time, nature of the doping anion and, the type of the electrolyte and the electrode material. CPs can grow on the electrode surface electrochemically without the need of an oxidant owing to their electrical conductivity [27].

Three different deposition routes are applied in electrochemical polymerization which involves direct oxidation of the corresponding monomer. These techniques employ application of i) a constant current (galvanostatic), ii) a constant potential (potentiostatic) and iii) a sweeping potential (potentiodynamic). So here there is no need of an oxidation agent. During the polymerization process, an anodic potential is applied to the monomer to get it oxidized onto the electrode and henceforth polymerization is initiated. The deposition process can continue until the applied potential is removed. Thus the polymer film thickness can be controlled by the polymerization time. One important disadvantage of electrochemical

polymerization is that large production scale is not possible as the working electrode area is limited [84].

## **2.1.2 Chemical Oxidative Polymerization**

Chemical oxidative polymerization is suitable for large-scale production of the CP in powdered form. This method is a quick and practical one to obtain the polymer in conducting form, and is performed in strong acidic aqueous medium (hydrochloric acid, sulphuric acid, formic acid.) like the electrochemical polymerization. Here, a dopant or an oxidant is required to initiate the process. The commonly used dopants are the oxidizing agents such as ammonium persulphate, ferric chloride, hydrogen peroxide and ceric nitrate. The primary role of the oxidant is to extract a proton from the aniline molecule without having to form a coordination bond with the intermediate or the final product [83].

### **2.1.2.1 Chemical Oxidative Polymerization of PANi**

Depending on the synthesis method, the electrical and morphological properties of synthesized PANi can differ. S. Bhadra et al. [85] performed both chemical oxidative and electrochemical polymerization for the synthesis of PANi keeping the temperature and composition same. It was revealed that the electrochemically synthesized PANi possessed lower conductivity and crystallinity, higher solubility and band energy, and larger particle size than that of the chemically oxidized PANi.

The saga of intrinsically conducting polymers has unfolded with the discovery of polyacetylene (PA) in 1958. But PANi is cheaper than PA endowed with easy synthesis process. The history of PANi is much older than the firstly reported polyacetylene and many other conducting polymers. In the year 1862, Dr. Henry Letheby, a professor working in the college of London Hospital, made a breakthrough by reporting the first ever synthesized a “blue substance” by electrolysis of aniline sulphate (AS), which changes color partly while coming under the influence of a reducing agent. In the early days, it was named as “aniline black” because of its dark black/green color, which was used for dyeing in textile sectors [86].

In 1910, Green and Woodhead performed controlled synthesis of PANi to discover its four oxidation states. This was followed by Jozefowic’s extensive study on the material [87]. Since then intensive research started on the potential applications of PANi in diverse fields.

Doping/dedoping controlled tunable electrical and electrochemical properties and diverse range of nano/microstructures of PANi facilitates its use in gas sensor, pH sensor, supercapacitors and fuel cell applications. Needless to say that PANi is one of the most desirable polymers among the CP family owing to its unique range of properties such as high thermal, electrical and environmental stability and its reasonable cost. Due to its rigid conjugation chain and brittle structure, the processing of PANi often becomes daunting. Hence for high-demanding applications, PANi must be teamed up with metal/metal oxide nanoparticles and other advanced materials such as graphene, carbon nanotubes to deliver the best results [88]. The covalent bond of the components of the nanocomposites makes PANi more stable for applications such as energy storage, catalysts systems etc [89].

Several past studies were devoted on synthesizing variety of PANi based nanostructures that make them suitable for novel sensor platforms and high density arrays to achieve advanced detection of varied classes of gases. Stejskal and co workers [90] synthesized PANi nanostructures and its derivatives by performing chemical oxidative polymerization in water. Ayad et al. carried out similar synthesis process to produce PANi and PPy nanotubes, nanoflakes, nanorods and nanoflowers [84], [91], [92] using diluted camphor sulphonic acid and acetic acid. A.A. Shah et al. [93] reported a cost effective chemical oxidative polymerization of PANi using diesel as a dispersion medium to use it as an anticorrosive coating for stainless steel. The synthesized PANi exhibited a highly porous morphology and good solubility, and remained stable upto 417<sup>0</sup>C.

Dan et al. [94] performed oxidative polymerization of PANi in formic acid medium with different reaction pathways and intermediates produced under the applied conditions. It was found that the reaction yield and the intrinsic viscosity of the polymer depended on the synthesis parameters. The base form of the PANi product showed stability upto 400<sup>0</sup>C and the acid form depicted pseudo-orthorhombic crystal structure. T. Yonehara et al. [95] undertook a convenient and low-cost method of utilizing naturally abounding sea water as the reaction solvent for synthesizing PANi. They confirmed the polarons of the synthesized PANi played the role of charge carriers. They further prepared PANi/silk composite in seawater to produce conducting cloth.

PANi is prepared by the oxidative or electrochemical reactions of aniline monomer in aqueous acidic medium. Chemical polymerization of PANi can yield a strikingly diverse class of morphologies ranging from single dimensional nanofibres, nanorods and nanotubes, two dimensional nanoflakes and three dimensional nanospheres and nanoflowers resulting from various proportions of oxidants, dopants and synthesis situations [96], [97]. Some of the commonly yielded morphology of PANi is shown in Fig. 2.1.

In most of the reported cases, emeraldine salt form of PANi (PANi-ES) was synthesised using oxidative polymerization of aniline monomer in aqueous acidic (organic or inorganic) medium. These monomers possess high electron donor properties and oxidation tendency. During the process, cations are produced in the monomer and the polymer growth is initiated with the formation of covalent bonds between the monomer units. The formation of the chain growth is accomplished in two ways – either through recombination of radical cation oxidation sites or electrophilic substitution. This yields a highly ordered chain structure of conducting PANi-ES consisting of regular assembly of more than 95% para-substituted aniline fragments linked in a head-to-tail configuration [24].

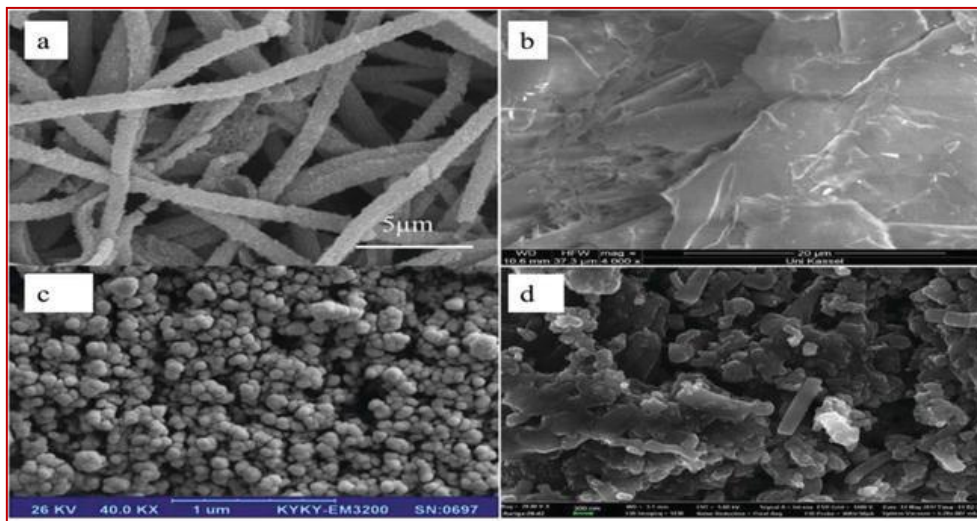


Fig. 2.1 SEM micrographs of different PANi nanostructures- a) fibres, b) smooth surface, c) globules and d) tubular [83].

In chemical oxidative polymerization, PANi is obtained by oxidation of aniline monomer with ammonium peroxydisulphate (APS) as the oxidant in an aqueous acidic medium. Salts of iron, cerium, silver, persulphates or dichromates are commonly used as oxidants having high oxidation potential ( $>+1.0V$ ) [24]. APS is more preferred due to its faster and easier

solubility [9]. APS has an oxidation potential of 2.01V and has the capability to oxidize all intermediate forms of the synthesis process.

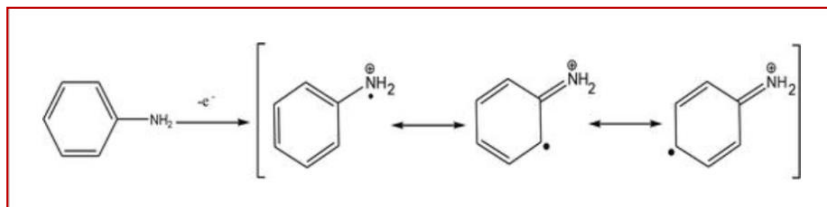


Fig. 2.2.a) Scheme 1: Oxidation of aniline during its polymerization [98].

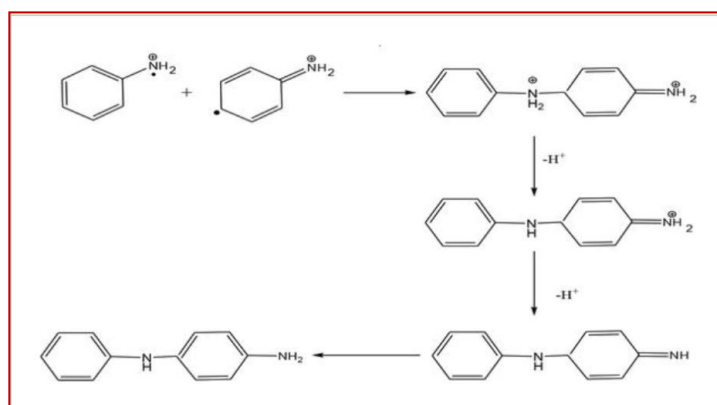


Fig. 2.2.b) Scheme 2: Formation of a dimer of aniline [99].

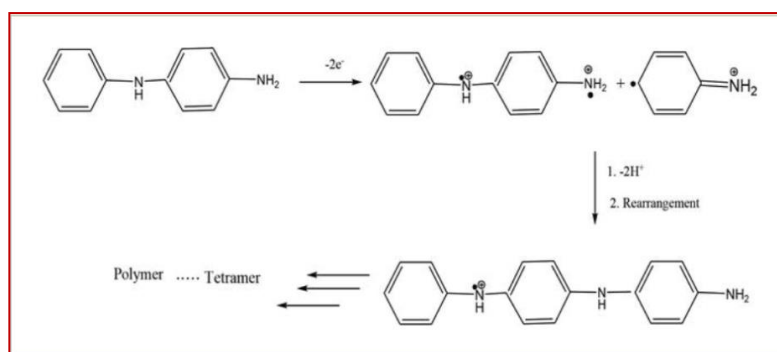


Fig. 2.2.c) Scheme 3: Formation of a trimer and formation of PANi [100].

The general mechanism of aniline oxidative polymerization is dominated by the radical reaction which can be subdivided into three steps, viz., i) initiation (Scheme 1), ii) chain

propagation (Scheme 2) and iii) termination (Scheme 3). Fig. 2.2 demonstrates scheme 1, 2 and 3 for the complete route of aniline polymerization using APS as the oxidant and hydrochloric acid (HCL).

In the induction period of aniline polymerization, aniline radical cations are created, which is followed by their recombination to give rise to a dimer. Subsequently, the oxidized terminal amino group of the polymer attacks the para-substituted monomer units [24].

The oxidative polymerization of aniline can take place under a wide range of acidic conditions with pH ranging from 14 to -1. But these give variety of polymerization results with the protonated products having conductivity varied from  $10^{-10}$  S/cm to  $10^2$  S/cm. A highly acidic medium results into the dark green conductive emeraldine salt. Aniline is protonated at  $\text{pH} < 3.5$  and gets positive charge. At the end, the entire polymer chain acquires a net positive charge. Aniline undergoes a complex, dynamic synthesis process with pH value constantly changing. It is important to find how quickly the pH value changes with changing different kinetic parameters and at what pH value, polymerization ends [24].

The oxidation process of aniline is exothermic and the temperature increases as the reaction proceeds. When an aniline molecule is added to the growing polymer chain, two hydrogen atoms are produced as protons and sulphuric acid as the by-product. So, the pH decreases during the reaction and the level of pH can be used to monitor the reaction progress [90].

At  $\text{pH} < 2.5$ , PANi with high molecular weight and high conductivity is achieved. At high pH, oligomers with low conductivity are formed. Thus at the end of polymerization, the polymer (high molecular-weight and high conductivity), oligomers and other oxidation products (low molecular-weight and low conductivity) of varied properties are yielded and together they are termed as PANi. Therefore, surface morphology of PANi thus synthesized often depicts a collection of two-dimensional micro spheres (oligomers) and two-dimensional nanotubes/nanofibres or three dimensional granules (PANi) [24].

## **2.2 Experimental: Preparation of CSA doped PANi-Ta<sub>2</sub>O<sub>5</sub> nanocomposite**

Aniline (Merck, 99%), camphor sulfonic acid (CSA, Merck) as acid dopant and ammonium peroxodisulphate (APS, Merck) as oxidant were used as received. All aqueous solutions were

obtained by mixing with right proportion of distilled water.

### 2.2.1 Synthesis of PANi-ES using chemical oxidative polymerization [75]

10 ml of aniline (0.1 mole) was added to 100 ml of hydrochloric acid (1M, pH=3.01) with vigorous stirring at room temperature. A light yellowish transparent aqueous solution of aniline was obtained accordingly. Another solution of the oxidizing agent was prepared by adding APS (0.0548 mole aqueous solution, 1.25gm), as oxidant, to 1M, 100 ml of hydrochloric acid. The APS solution is added drop-wise to a stirred solution of the aniline solution, pre cooled to 3-5<sup>0</sup> C. This is an exothermic reaction. So APS solution is added very slowly to prevent the warming of the solution over a period of 30 minutes with vigorous stirring. The reaction is carried out in the presence strong acid such as 1M HCL because low pH promotes the head-to-tail coupling of aniline monomers [100]. A dark green precipitate continues to form after 10 to 20 minutes of stirring. The mixture is stirred in a magnetic stirrer continuously for 4 hours to ensure completion of the reaction. Finally, the solution is filtered, washed with distilled water repeatedly and hydrochloric acid till the filtrate turns to be completely colorless. The precipitate remained on the filter paper is a dark green material which is the emeraldine salt form of PANi (PANi-ES). The precipitate is collected, dried in oven at 60<sup>0</sup> degree for 1 hour which yielded the green colored emeraldine salt. The PANi-ES thus obtained was photographed as shown in Fig. 2.3.

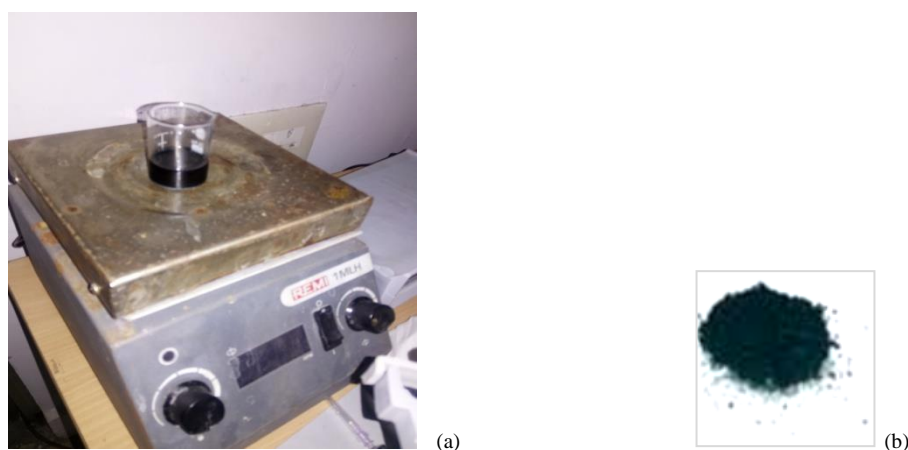


Fig. 2.3. a) Photograph of dark green precipitate formation of PANi-ES, b) Filtered, dried and ground PANi-ES in powdered form.

Polyaniline base was obtained when the emeraldine salt was stirred with 0.1M aqueous solution of ammonia for 6-8 hours, filtered and washed with distilled water to obtain

emeraldine base (PANi-EB). PANi-EB in a dark blue color was obtained and then dried in oven at 60<sup>0</sup> degree for 1 hour which yielded the emeraldine base in powdered form.

### 2.2.2 Synthesis of CSA doped PANi (ES)-Ta<sub>2</sub>O<sub>5</sub> nanocomposite [75]

PANi-ES is mixed with tantalum pentoxide nanopowder (Ta<sub>2</sub>O<sub>5</sub>) in 50 wt% and grinded in a mortar for 1 hour to get a fine powder of PANi-Ta<sub>2</sub>O<sub>5</sub>. The CSA doped PANi-Ta<sub>2</sub>O<sub>5</sub> nanocomposites were obtained by adding CSA (salt like solid powder) in 20 wt%, 30 wt% and 40 wt% to the already prepared PANi-Ta<sub>2</sub>O<sub>5</sub> and then grinded in a mortar for solid-state doping. Table 2.1.a and 2.1.b [75] show the various proportions of Aniline, APS and HCL to prepare emeraldine salt form of PANi, and the proportions of PANi (ES), Ta<sub>2</sub>O<sub>5</sub> and CSA used to prepare the nanocomposite samples.

Table- 2.1.a

(Sample Details- PANi)

Sample	Aniline	APS	HCL
PANi (Emeraldine salt)	0.1 mole (10 ml)	0.05 mole (1.25 gm)	1 mole, 100 ml for each Solution

Table- 2.1.b

(Sample Details- PANi nanocomposites)

Nanocomposite with constituents	Sample Name	PANi	Ta <sub>2</sub> O <sub>5</sub> (50wt%)	CSA	Total weight of the sample
PANi	PANi	1 gm			1 gm
PANi-Ta <sub>2</sub> O <sub>5</sub> (50wt%) Nanocomposite	PANi-Ta <sub>2</sub> O <sub>5</sub>	1 gm	0.5gm		1.5 gm
PANi-Ta <sub>2</sub> O <sub>5</sub> doped with 20wt% CSA	PANi-Ta <sub>2</sub> O <sub>5</sub> -CSA20%	1 gm	0.5gm	0.2 gm	1.7 gm
PANi-Ta <sub>2</sub> O <sub>5</sub> doped with 30wt% CSA	PANi-Ta <sub>2</sub> O <sub>5</sub> -CSA30%	1 gm	0.5gm	0.3 gm	1.8 gm
PANi-Ta <sub>2</sub> O <sub>5</sub> doped with 40wt% CSA	PANi-Ta <sub>2</sub> O <sub>5</sub> -CSA40%	1 gm	0.5gm	0.4 gm	1.9 gm

## **2.3 Characterization of CSA doped PANi-Ta<sub>2</sub>O<sub>5</sub> nanocomposite**

### **2.3.1 Electron Microscopy (SEM and TEM): Theory and Principle**

Electron microscopy has been a revolutionary imaging tool for enabling characterization of nanomaterials to capture their unique properties. It can provide much higher resolution than optical microscope, offering information which is otherwise not possible to gather. Light microscopy provides a resolution limited to 0.1.μm (100 nm). An electron microscope designed to operate at 200-300 keV can offer an image spatial resolution down to less than 0.1 nm (100 pm).

High accelerating voltage can produce shorter-wavelength, high-energy electrons. These short-wavelength, highly energized electrons interact more strongly with nanomaterials and thus can produce high resolution images.

The two most common types of electron microscopy are scanning electron microscopy (SEM) and transmission electron microscopy (TEM). SEM and TEM differ on the technique they employ to capture the image and the types of images they can produce.

The key advantages of electron microscopy over light microscopy is the capability of producing high-resolution image over a wide magnification range 10-500,000 times for SEM and 1-2000 million times for TEM. Another important advantage of electron microscopy is the use of electrons instead of light. Electrons having negative charge interact very strongly with atoms. This leads to the generation of emission of signals encompassing a wide range of phenomena. These signals can be detected and use to construct valuable structural and chemical images of specific areas of the sample.

The major disadvantage of electron microscopy is the need for vacuum for operation. Electrons interact with air molecules and sufficient nos. of electrons of the electron beam will be scattered. To avoid this, some degree of vacuum is needed for operation of EM. Typical pressures needed for vacuum (low) in SEM is 0.1 – 10<sup>-4</sup> Pa and 10<sup>-4</sup> to 10<sup>-7</sup> Pa (high vacuum) for TEM [101]. A high vacuum can come in conflict with the properties of the sample material particularly the liquids and biological materials. Also, the high kinetic energy of the incident electron can induce damage material properties of the specimen. To combat these

difficulties, special variable pressure and environmental electron microscopes have been developed [102].

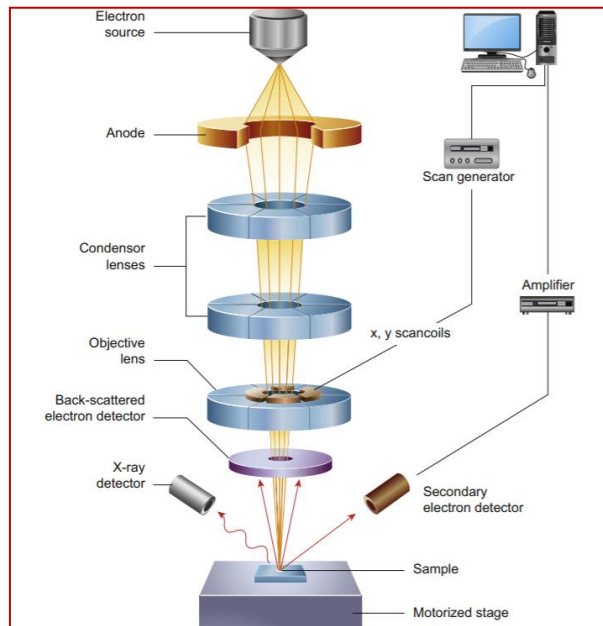


Fig. 2.4.a) Schematic of SEM imaging with key components [102].

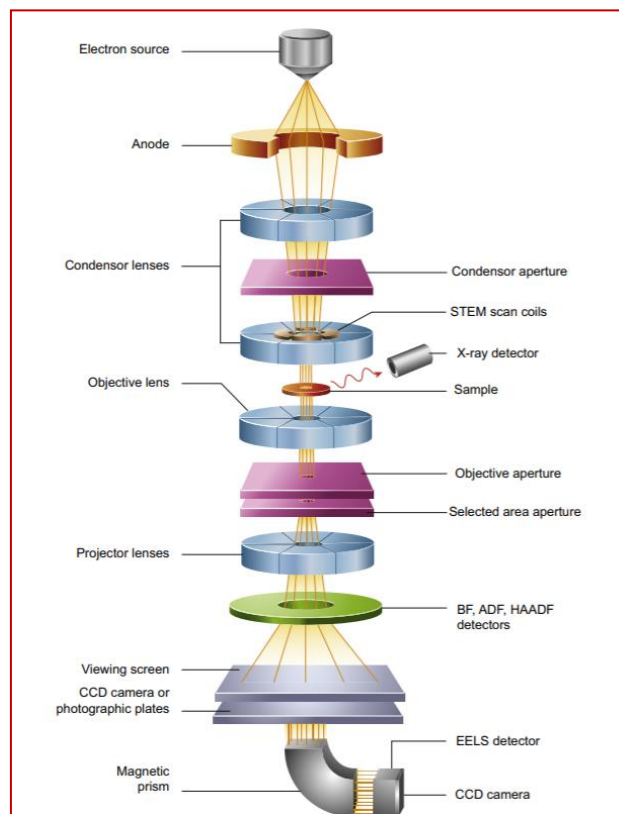


Fig. 2.4.b) Schematic of TEM imaging with key components [101].

The schematics of SEM and TEM imaging system are shown in Fig. 2.4. Both SEM and TEM microscopes generate highly focussed electron beams that strike the specimen inside a vacuum chamber. But SEM microscopes are designed primarily to study the material surface of the specimen, while TEM microscopes are primarily designed to study the internal structure of the material.

Scanning electron microscopy scans the sample surface with a high intensity electron beam in a raster scan pattern. The primary electron beam is produced under high vacuum and it scans the surface of the specimen in a rectangular raster. On striking the specimen by the electron beam, a varied signal produces an image of the surface or the elemental composition along with secondary electrons, backscattered electrons and energy dispersive X-rays (EDX). The microscope records the information gathered from the interaction between the electrons and the sample [101].

TEM microscope uses a broad beam of electrons to produce an image of the sample's internal structure. A beam of electron is incident onto a defined area of the sample surface and penetrates through the sample. These beams are focussed by lenses and collected by a parallel detector to form the image. Electron energies in TEM are much intense than SEM, typically 80-300 keV, to make them to penetrate through the specimen. A high resolution image is finally created with sample's morphology, structural composition and crystallinity [101].

There are many similarities between SEM and TEM in regards to the high-resolution microscope they use. The microscope used by each method comprises of an electron gun that produces the electron stream towards a sample kept in vacuum, and each method uses lenses and electron apertures to confine the electron beam and generate the image. Differences in functioning of the two methods are vast such as how do they work, the nature of the samples they require and the resolution of the images they create [102].

### **2.3.2 X-Ray Diffraction (XRD): Theory and Principle**

The research on X-ray diffraction (XRD) by crystals was embarked upon with the studies initiated by Laue, Freidrich and Knipping in 1912. This paved numerous paths for the study of crystalline materials. Over the years, these methods have been progressed far towards powerful tools in various fields of crystallography.

The XRD methods exploit the ability of crystals to diffract X-rays in a characteristic manner and this allows a thorough study of the crystal structure. The recorded diffraction patterns provide valuable insight of different micro and macro structural features of the sample. By examining the peak position of the diffractions patterns, lattice parameters, chemical composition, qualitative phase analysis can be studied. By the peak intensity, information about the crystal structure such as atomic positions, texture and quantitative phase analysis can be derived. Based on the peak shape, deformations and crystallite size can be obtained [103].

X-rays are high-frequency electromagnetic waves having wavelength ranging between  $10^{-3}$  to  $10^1$  nm. In some conventional methods, X-rays are produced by generating electrons by heating tungsten filament in a vacuum and then accelerating them through a high potential to strike a target to emit the X-rays.

X-ray emission in synchrotrons is based on a different principle. High-energy electrons are generated by a high-power electron gun and are then accelerated by injecting the electrons in a booster ring. The electrons are then driven to a storage ring where the X-ray radiation is obtained. XRD methods, in general, use only the characteristic radiation with the highest intensity, that is, the  $K\alpha$  radiation and remove most of the other radiations by applying appropriate filters.

When X-ray strikes the matter, a no. of interactions take place leading to different absorption and scattering effects. Due to the periodic nature of the crystalline structure, constructive or destructive scattering outputs are obtained that enable the investigation of the crystal structure [103].

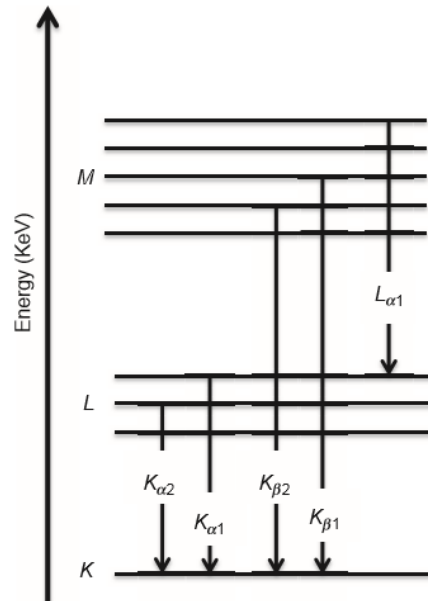


Fig. 2.5. Schematic of various atomic energy levels and characteristic emission of X-ray radiation [104].

The principle of XRD methods is based on the diffraction of X-rays by periodic atomic plans and the angle of the diffracted signals. The various atomic energy levels of the characteristic X-ray emissions are shown in Fig. 2.5. The geometrical interpretation of the XRD principle is provided by W.L. Bragg in 1913. Bragg’s law is given by the following equation.

$$N\lambda = 2d_{hkl} \sin(\theta) \quad (2.1)$$

In equation 2.1,  $n$  is the order of diffraction,  $\lambda$  is the wavelength of the incident beam in nm,  $d_{hkl}$  is the lattice spacing in nm and  $\theta$  is the angle of diffraction in degree. These parameters are illustrated in Fig. 2.6.a. In a polycrystalline material with fine grains, diffraction occurs for each lattice planes resulting in the formation of diffraction cones that appears in the form of diffraction rings or Debye rings if detected by a plane detector as shown in Fig. 2.6.b.

The diffracted data is represented as the intensity distribution as a function of  $2\theta$ . The information which can be extracted is represented in the Fig. 2.7.

Performing the background subtraction, maximum value of peak intensity,  $I_{max}$  and the area covered under the peak,  $I_{int}$  can be defined. The peak position can be estimated by different

methods such as center of gravity, fit of different mathematical functions etc. The peak width can be characterized by the FWHM (full width half maximum).

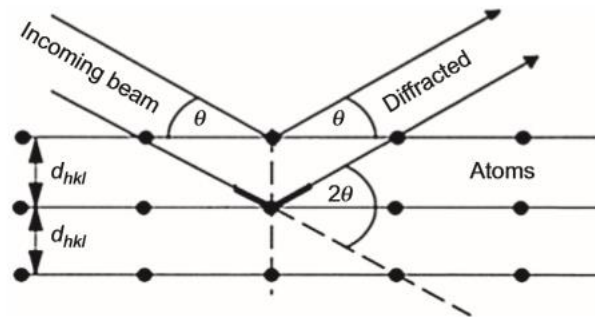


Fig. 2.6.a) Geometric condition for diffraction from the atomic planes [103].

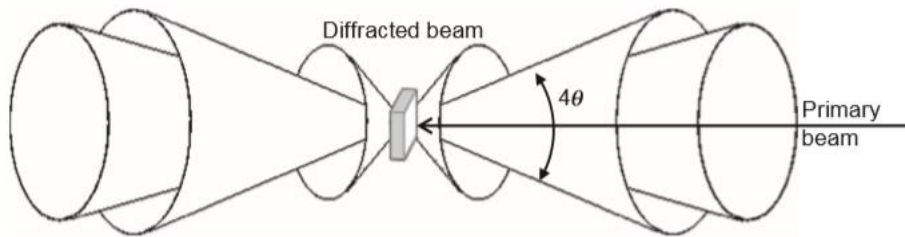


Fig.2.6.b) Diffraction cones formed in the diffraction for polycrystalline material [103].

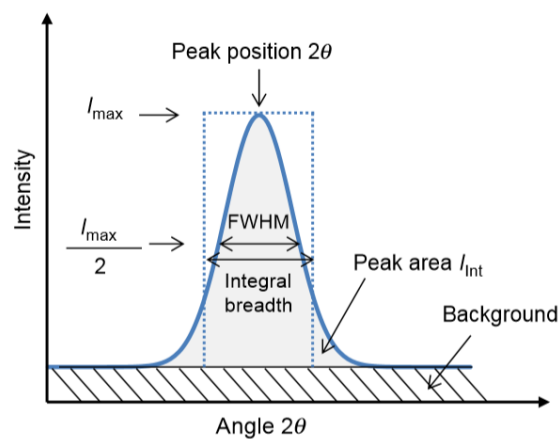


Fig.2.7. Diffraction peak and different associated information [103].

### 2.3.3 Ultra Violet and Visible (UV-Vis) Spectroscopy study- Theory and principle

UV-Vis spectroscopy is an important analytical instrument that has been used extensively in modern day laboratories. This method has surpassed its competitors by virtue of its simplicity, versatility, accuracy, speed and cost-effectiveness. Its main use find in quantitative determination of different organic and inorganic materials in solution.

The basic idea behind any spectroscopy technique is related to the interaction of light with matter. When light is absorbed by the matter, there is an increase in energy level of the atoms or molecules. The absorption of light in visible or ultraviolet range of electromagnetic spectrum by a chemical compound will produce a distinct spectrum. On ultraviolet radiations absorption, the electrons are elevated from the ground state towards a higher energy state. The energy absorbed from ultraviolet radiations is equal to the difference in energy between the higher energy level and the ground state [104].

Radiation is the external manifestation of energy and we constantly feel its existence through our senses of sight and touch. It can be considered as a waveform with a wavelength  $\lambda$  as shown in Fig. 2.8. The frequency,  $\nu$  is the no. of peaks passing through a point per second. The following relation can be written using the above terms.

$$c = \nu \cdot \lambda \quad (2.2), \text{ where } c \text{ is the velocity of light in a vacuum.}$$

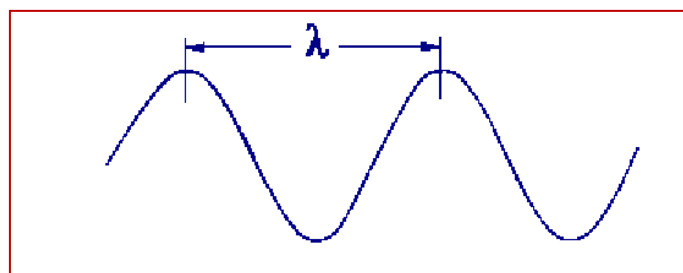


Fig. 2.8. The waveform of electromagnetic spectrum and its wavelength  $\lambda$  [104].

The full electromagnetic spectrum is continuous and each merges into the next smoothly. For spectroscopy, the parts of spectrum in ultraviolet and visible regions are considered with

wavelength expressed in nanometers (nm) according to equation 2.3. The electromagnetic spectrum with the respective wavelengths is shown in table 2.2.

$$1\text{nm} = 10\text{\AA} = 10^{-9}\text{ meters} \quad (2.3)$$

Table- 2.2

(The electromagnetic spectrum and the respective wavelengths)

Region of the electromagnetic spectrum	Wavelength (nm)
Far ultraviolet	10-200
Near ultraviolet	200-380
Visible	380-780
Near infrared	780-3000
Middle infrared	3000-30,000
Far infrared	30,000-300,000
Microwave	300,00-1,000,000,000

The internal energy of a molecule of any substance is the sum of the energy of its electrons, the vibration energy between the constituent atoms and the energy pertaining to the rotation of the molecule. The electronic energy levels of simple molecules are widely spaced and with the absorption of a high energy photon, a molecule can be excited from one level to another.

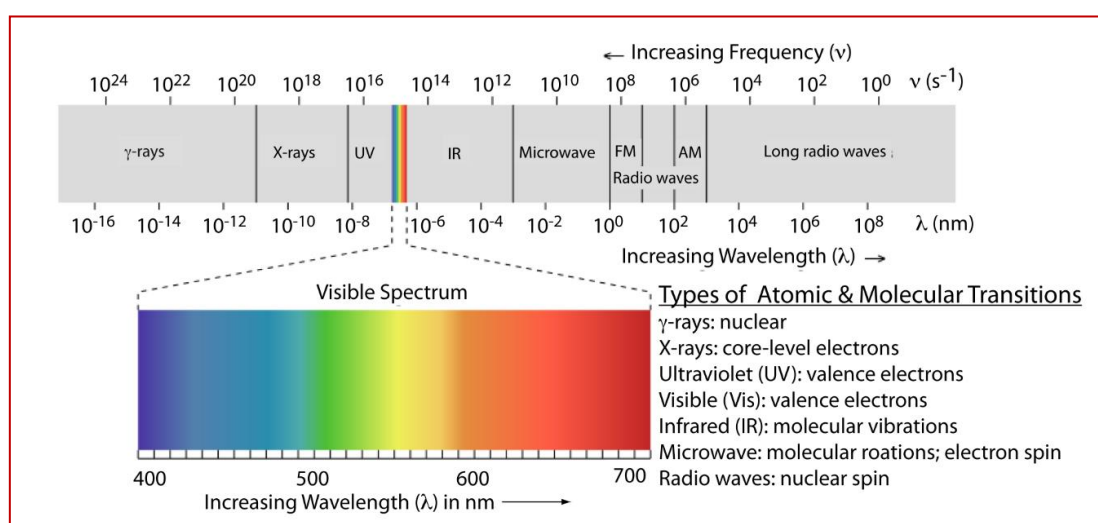


Fig. 2.9. The electromagnetic spectrum with the boundaries of different regions and the type of atomic/molecular transitions due to change in energy [105].

The electromagnetic spectrum and the respective atomic/molecular transitions are illustrated in Fig. 2.9. The electronic energy levels of simple molecules are widely separated and usually only the absorption of a high energy photon, that is one of very short wavelength, can excite a molecule from one level to another. In case of complex molecules, the energy levels are more closely packed. So, photons of near ultraviolet and visible light can influence the transition. These molecules can, therefore, absorb light in the areas of near ultraviolet and visible regions.

The vibration energy states of a molecule are much closely spaced than the electronic energy levels. Therefore, photons of lower energy can bring about vibration changes. Light absorption due to only vibration changes can take place in the infrared region. The rotational energy states of molecules are also very closely spaced that light in the far infrared and microwave regions have enough energy to result these small changes.

For ultraviolet and visible waveforms, the absorption spectrum (a plot of its degree of absorption against the wavelength of the incident radiation) of a molecule should show a no. of very sharp lines. Each line should appear at a wavelength where the energy of an incident photon matches with the energy required to excite an electronic transition. But in practice, these spectra for most of the molecules consist of a few humps instead of sharp lines. These humps indicate that the molecule is absorbing radiation over a band of wavelengths. One reason for this band is that an electronic level transition is usually accompanied by a simultaneous change among numerous vibration levels [104]. These features can be seen in Fig. 2.10.

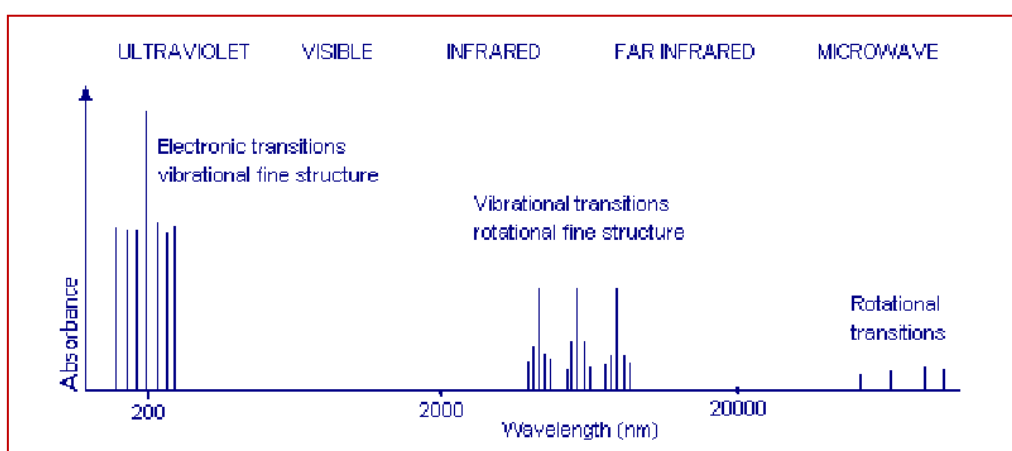


Fig. 2.10. An ideal UV-Vis absorption spectrum [104].

Also, each of the several vibration levels associated with the electronic states does also have many rotational levels associated with it. The contribution of the rotational changes to the transition results in filling in the gaps in the fine structure due to vibration changes.

In UV-Vis spectroscopy, chemical compounds are prepared in solution. In solution, the molecules are closely packed together, influencing each other by disturbing the almost infinite nos. of energy levels and transform the sharp lines into bands. At high temperature or pressure, even the electronic bands of solutions can blur to give rise to single wide bands [104]. The UV-Vis spectra of benzene in vapour and solution phase are shown in Fig. 2.11.

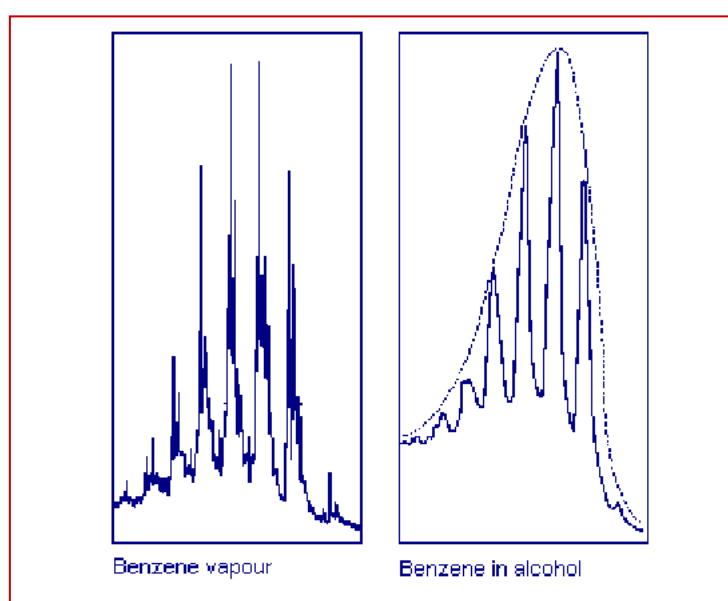


Fig. 2.11. Spectra of benzene in its vapor and solution phase [104].

A molecule exhibits absorption spectra in the visible or ultraviolet region when radiation causes a transition in electronic levels within the structure. The energy provided by light promotes electrons to excite from ground state orbitals to higher energy orbitals.

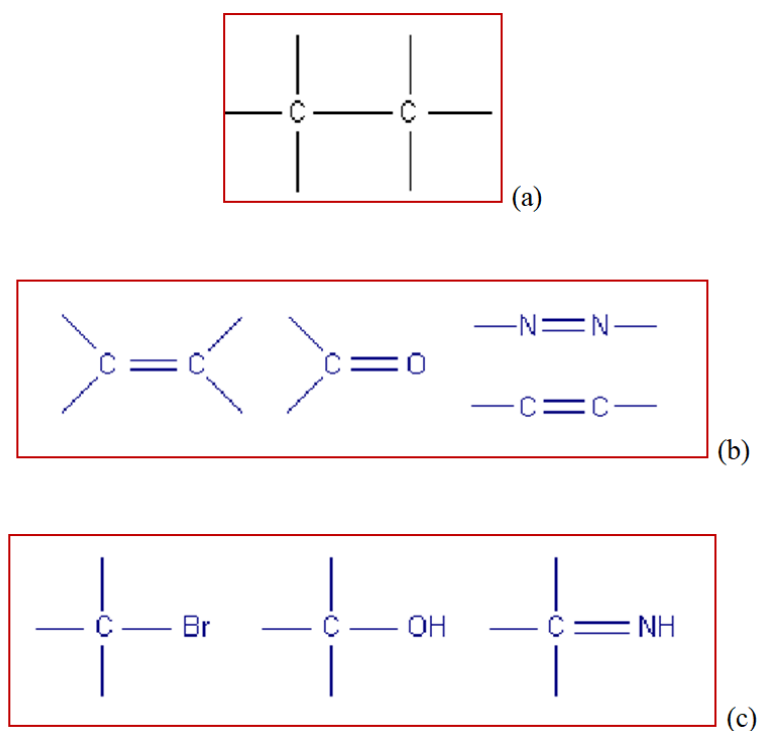


Fig. 2.12. Various molecular orbitals in carbon compounds: a)  $\sigma$  — molecular orbital, b)  $\pi$  — molecular orbital and, c) n (non-bonding) molecular orbital [104].

Bonding molecular orbitals are of lower energy than the atomic orbitals from which they are formed. Bonding molecular orbitals are those where the electrons spend most of their time directly between the two nuclei.

Antibonding molecular orbitals are of higher energy than the atomic orbitals from which they are formed. There are, particularly, three bonding molecular orbitals. Sigma ( $\sigma$ ) molecular orbital are symmetrical about the axis of the bond. The pi ( $\pi$ ) bonding is a side to side overlap of orbitals, which causes electron density nil along the axis, but there is electron density above and below the axis [104]. The various molecular orbitals of some example carbon compounds are depicted in Fig. 2.12. In addition of these three, two types of antibonding orbitals may come into play in the transitions, viz.,  $\sigma^*$  orbital and  $\pi^*$  orbital. The relative placing of these molecular orbitals along the energy axis are shown in Fig. 2.13.

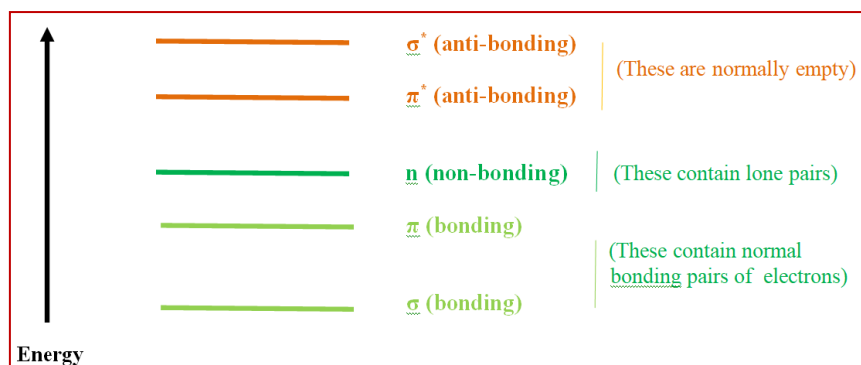


Fig. 2.13. Relative energy levels of bonding and anti-bonding molecular orbitals [106].

The electronic transitions as shown in Fig. 2.14 may occur during the absorption of ultraviolet and visible light – a)  $\pi$  to  $\pi^*$ , b)  $\sigma$  to  $\sigma^*$ , c)  $n$  to  $\pi^*$ . Transitions of the type  $n$  to  $\pi^*$  and  $\pi$  to  $\pi^*$  occur in molecules with unsaturated centers. They need less energy and occur at longer wavelengths than transitions to  $\sigma^*$ . The  $\sigma$  to  $\sigma^*$  transition requires energy of a photon having a wavelength not lying in the UV-Vis range. Thus only  $\pi$  to  $\pi^*$  and  $n$  to  $\pi^*$  are observed in the UV-Vis range.

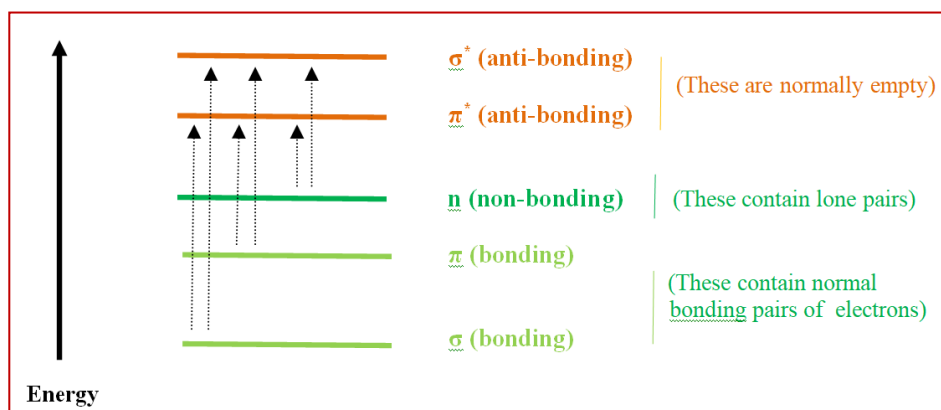


Fig. 2.14. Electronic transitions of molecular orbitals caused by UV/Visible light [106].

UV-Vis absorptions are observed between 200 to 350 nm for colorless compounds and from 350 to 1000 nm for colored compounds or dyes. The wavelength of absorption spectra depends on the length of the pi-conjugation system. The highly conjugated organic compounds show absorption in the UV-Vis region of 350 to 800 nm [107].

### **2.3.4 Fourier Transform Infrared Spectroscopy (FTIR) -Theory and principle**

FTIR spectroscopy has been an excellent tool for non-destructive qualitative analysis of materials in the laboratory for over seventy years. The FTIR method is used to identify organic, inorganic (in some cases) and polymeric materials and it relies on infrared light to scan a given sample and observe the composition of the material including unknown components, different bonds and hence different functional groups. The FTIR spectrometer produces a graph depicting degree of absorbance or transmittance against wave numbers. The absorption spectrum reveals a no. of peaks representing the components present. The absorbance peaks indicate functional groups like alkanes, ketones, acid chlorides etc. Different functional groups absorb infrared radiations of different wavelengths. Thus FTIR absorption spectrum produces a fingerprint of a sample with the absorption peaks corresponding to the frequencies of vibrations between the bonds of the atoms constituting the material. Also, the size of the peaks in the spectrum can directly indicate the amount of material present [108].

FTIR testing methods can analyse samples in solid, liquid, powder form or in thin film using following methods.

- Solids placed on a crystal - attenuated total reflectance (ATR).
- Liquids placed between two sodium chloride plates – Nujol.
- Thin film placed in a cassette.
- Powdered sample mixed with potassium bromide (KBr) and placed in a KBr pellet.

Before starting the FTIR analysis, the sample is prepared either by using ATR, Nujol or other technique. The resultant spectrum is compared in a reference library program to identify components or to find the best match for an unknown component.

FTIR method is preferred over other dispersive or filter methods of infrared spectral techniques because of its precision, high scanning speed and high optical throughput, sensitivity, simplicity in mechanical set-up [108].

An interferometer is a simple optical device that can produce a unique signal having all of the infrared frequencies encoded into it. The signal can be measured on the order of one second or so. The resulting signal is called interferogram as shown in Fig. 2.15.

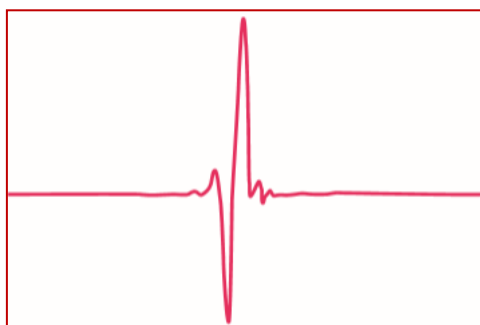


Fig. 2.15. Interferogram (signal produced by the interferometer) [108].

The resulting signal is called an interferogram which has the unique property that every data point (a function of the moving mirror position) which makes up the signal has information about every infrared frequency which comes from the source. This means that as the interferogram is measured all the frequencies are being measured simultaneously. Thus, the use of the interferometer results in extremely fast measurements. Because the analyst requires a frequency spectrum (a plot of the intensity at each individual frequency) in order to make an identification, the measured interferogram signal cannot be interpreted directly. A means of “decoding” the individual frequencies is required. This can be accomplished via a well-known mathematical technique called the Fourier transformation. This transformation is performed by the computer which then presents the user with the desired spectral information for analysis as shown in Fig. 2.16 [108].

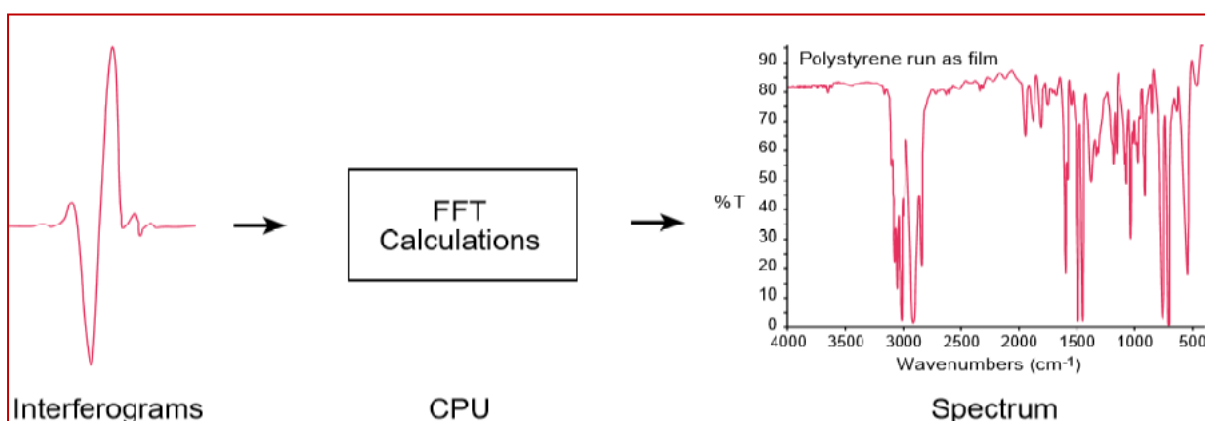


Fig. 2.16. Conversion of interferogram signal to FTIR spectrum using Fast Fourier Transform (FFT) [108].

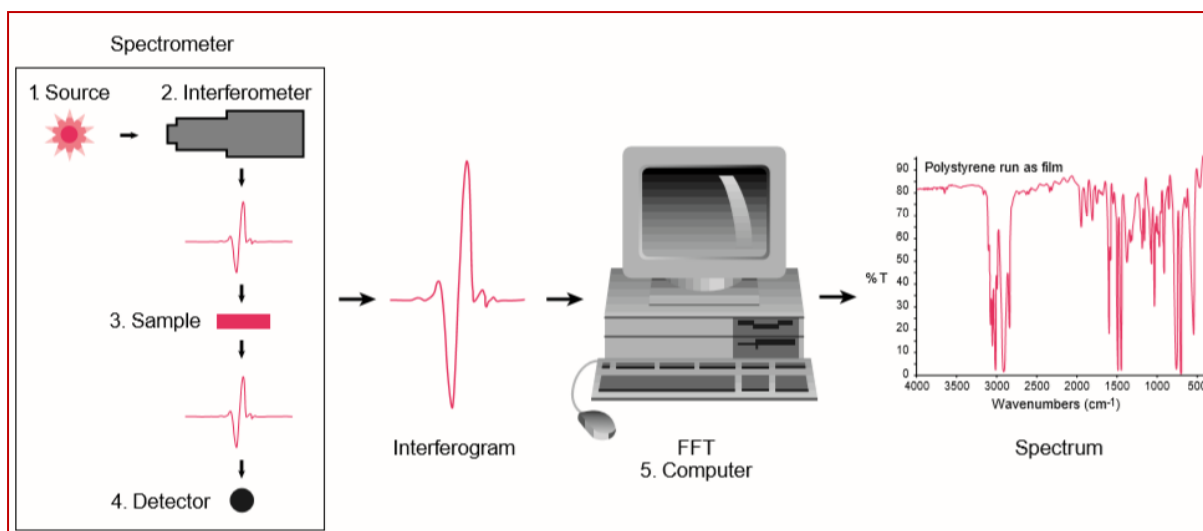


Fig. 2.17. Use of spectrometer to produce FTIR spectrum [108].

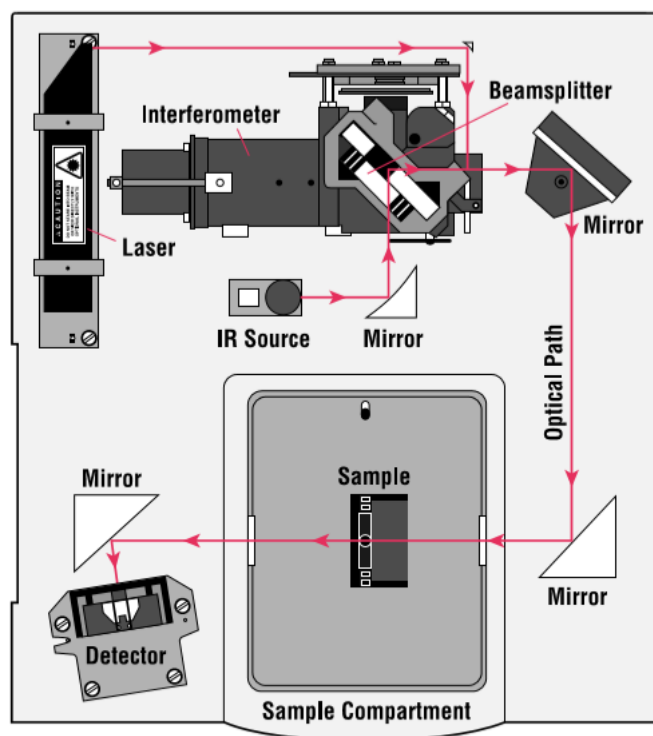


Fig. 2.18. A simple schematic of a spectrometer [108].

As the interferogram is measured, all frequencies are also being measured simultaneously. Thus, the interferometer can handle extremely fast measurements. From the analyst's point of view, a frequency spectrum (a plot of degree of intensity against each individual frequency) is desirable in order to identify a component. The interferogram signal cannot be directly

used. So, a decoding process is needed where a well-known mathematical tool called Fourier Transform is employed. Here, each individual frequency is subjected to Fast Fourier Transform (Fig. 2.16 and 2.17) using computer to create the desired FTIR spectrum for analysis. The schematic of a spectrometer is shown in Fig. 2.18.

## 2.4 Instrumentations used

Surface morphology of the synthesized CSA doped PANi-Ta<sub>2</sub>O<sub>5</sub> samples were characterized by (i) Scanning Electron Microscopy analysis using a [ZEISS SIGMA VP \(variable pressure\) field emission scanning electron microscope \(FE-SEM\)](#), (ii) Transmission Electron Microscopy was performed using [JEM-2100](#), (iii) powder XRD spectra of the samples were obtained using X-ray diffraction ([XRD, Brukers AXS, Germany/D8 Focus](#)) with Cu-K $\alpha$  radiation, beam wavelength=1.54Å operated at 40KVA/40m within the range of 10-85<sup>0</sup> (2 $\theta$ ), (iv) UV-Visible spectra of the PANi samples dispersed in m-cresol were recorded using [Perkin Elmer Lambda-35](#) UV-Vis spectrometer over the wave number range of 300–700 nm, (v) FTIR spectroscopy analysis was performed using [Nicolet 6700](#) spectrometer over the wave number range of 4000–500 cm<sup>-1</sup>. The spectra of the powdered nanocomposites were taken using [Attenuated Total Reflectance \(ATR\) Sampling Accessory](#).

## 2.5 Results and discussion

### 2.5.1. Scanning Electron Microscopy (SEM)

PANi can demonstrate a wide variety of morphological structures depending on the synthesis condition, proportions of oxidants and dopants as discussed earlier. The most common morphology of PANi in powdered form is the granular or globular structure that is resulted from precipitation oxidative polymerization under strong acidic conditions at pH < 2.5.

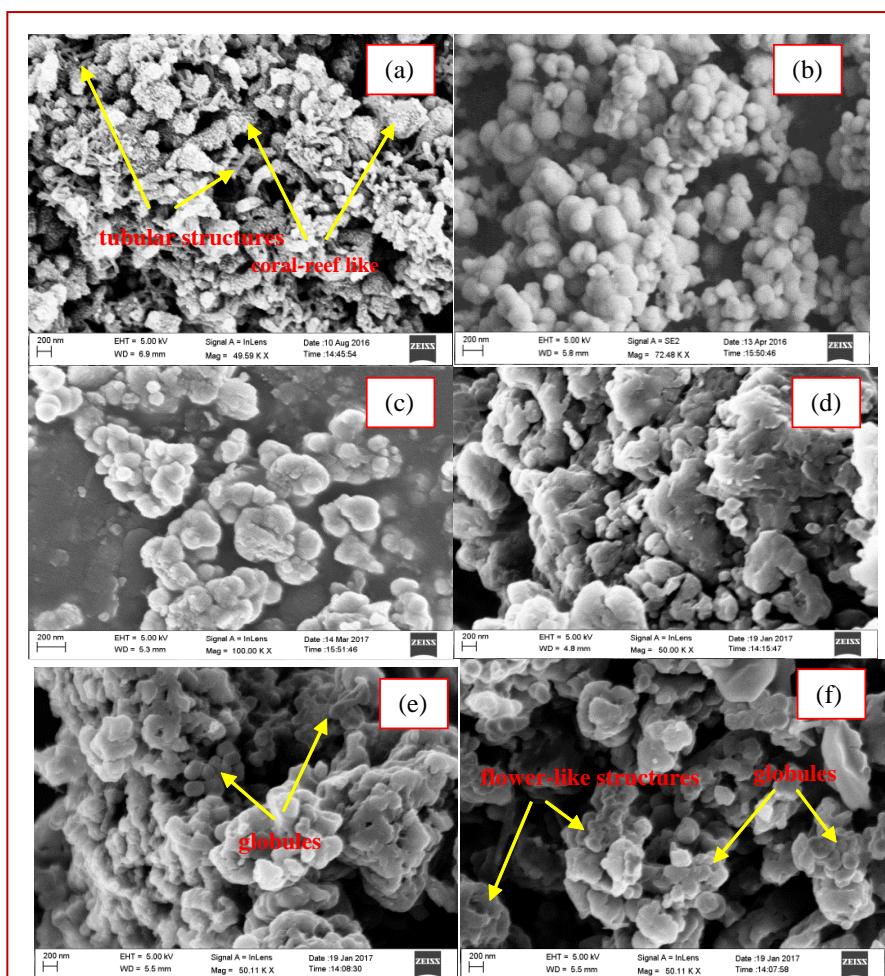


Fig. 2.19. FESEM of (a) PANi, (b) Ta<sub>2</sub>O<sub>5</sub>, (c) PANi-Ta<sub>2</sub>O<sub>5</sub>, (d) PANi-Ta<sub>2</sub>O<sub>5</sub>-CSA20%, (e) PANi-Ta<sub>2</sub>O<sub>5</sub>-CSA30%, (f) PANi-Ta<sub>2</sub>O<sub>5</sub>-CSA40% [75].

The SEM micrographs of pure PANi, PANi-Ta<sub>2</sub>O<sub>5</sub> and CSA doped PANi-Ta<sub>2</sub>O<sub>5</sub> nanocomposites are presented in Fig.2.19. As clearly observed in Fig. 2.19.a, pristine PANi possessed a no. of non-uniform, aggregated globular structures with a good quantity of nanotubes dispersed in it. The aggregation resulted in coral-reef like structures at some places. In Fig. 2.19.b, well defined globular shaped morphology can be observed for Ta<sub>2</sub>O<sub>5</sub>.

The transition of non-conducting aniline oligomer without the conjugation chain to the conducting polymer with the formation of the conjugation chain resulted in the formation of tubular structures. Such morphology is observed when PANi synthesized in the presence of acids of pH of 1 to 4.5 [24]. The appearance of coral-reef like structure may be attributed to the use of lower molar concentration of aniline or a moderate oxidant in the polymerization process [109]. The nanofibrous structures possess high surface area, small diameter and porosity which can enhance the diffusion of analyte gas molecules into the sensing material, causing high sensitivity and short response time [110].

PANi-Ta<sub>2</sub>O<sub>5</sub> nanocomposite depicts several non-uniform but prominent clusters of well-formed **spherical nanoparticles** (Fig.2.19.c). Due to the increased agglomeration, it is difficult to find the exact size of the nanoparticles. This type of spherical nanostructures possess greater surface to volume ratio, making them suitable for gas sensing.

The agglomeration of the nanoparticles augmented with the increased doping percentage of CSA as seen in Fig. 2.19.d to 2.19.f. The size of the globules measured as +200 nm diameter. It can be observed the formation of some **flower-like structures** as a result of increased aggregation of the nanoparticles as seen in Fig. 2.19.f. These kinds of structures can lead to greater crystallinity which is desirable for good sensing applications [111].

During synthesis process, the aniline monomer and the dopant aggregated to form mesostructures that caused the growth of flower like nanostructures. These PANi nanostructures have been reported to have improved features like high conductivity, large surface area and light weight compared to the bulk polymer [97].

## **2.5.2 Transmission Electron Microscopy (TEM)**

TEM uses electrons which are passing through the sample to create the image, while SEM produces the image by detecting the reflected electrons. Therefore, more detailed material information can be extracted from TEM analysis such as the crystal structure of the sample, morphology and stress state information, while SEM images provide information of the sample surface and its composition. Another important difference between SEM and TEM is the optimal spatial resolution that they render. SEM resolution is limited to ~0.5 nm, while the recent aberration-corrected TEM can offer resolution less than 50 pm [113].

The selected area electron diffraction (SAED) pattern is a crystallographic experiment that can be performed inside a transmission electron microscope. SAED is an important technique to determine the crystal structure of any material. It is a complementary technique in TEM where the electrons are diffracted at a selected area and bright spots with dark background are resulted accordingly. SAED pattern provides valuable information of a material – whether it is single crystalline, polycrystalline or amorphous.

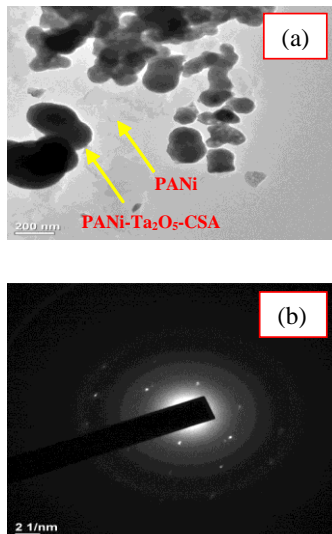


Fig. 2.20. a) TEM micrograph of PANi–Ta<sub>2</sub>O<sub>5</sub>-CSA40%, b) SAED pattern of the nanocomposite [75].

The TEM micrograph of PANi–Ta<sub>2</sub>O<sub>5</sub>-CSA40% nanocomposite is depicted in Fig.2.20.a. It reveals the formation of aggregated structures of globules which are dispersed in the PANi matrix. The globules possessed non-homogeneous roundish shapes with an average diameter of 180 nm-200 nm. Fig.2.20.b shows the selected area diffraction pattern (SAED) pattern of the sample. The ring patterns were created by the fine granules of the polycrystalline nano material. The small bright spots constitute the rings and each spot originates from Bragg reflection from an individual crystallite.

### 2.5.3 X-Ray Diffraction (XRD) analysis

In general, a polymer chain is comprised of both amorphous and crystalline realms. PANi backbone is quite stiff due its linear structure and chain bending is difficult. Therefore, it is hard to obtain a crystalline domain. Undoped PANi is normally highly amorphous. Doping and addition of inorganic oxides into the polymer matrix may cause significant changes, inducing a crystalline domain.

The XRD patterns of the PANi, PANi-Ta<sub>2</sub>O<sub>5</sub> and PANi-Ta<sub>2</sub>O<sub>5</sub>-CSA40% nanostructures are shown in Fig.2.21. Pure PANi revealed one broader diffraction peak at  $2\theta=20.68^\circ$  corresponding to (201) plane and one sharp and distinct peak at  $2\theta=25.24^\circ$  corresponding to (300) plane. These peaks are indexed in tetragonal crystal system using commercially

available Powder Diffraction software (POWD). The lattice parameters are  $a=10.6687\text{\AA}$ ,  $c=7.0465\text{\AA}$  and  $c/a=0.6605$ . The intense peak at  $2\theta=25.24^\circ$  having Miller indices (300) reveals crystal growth in the direction [300].

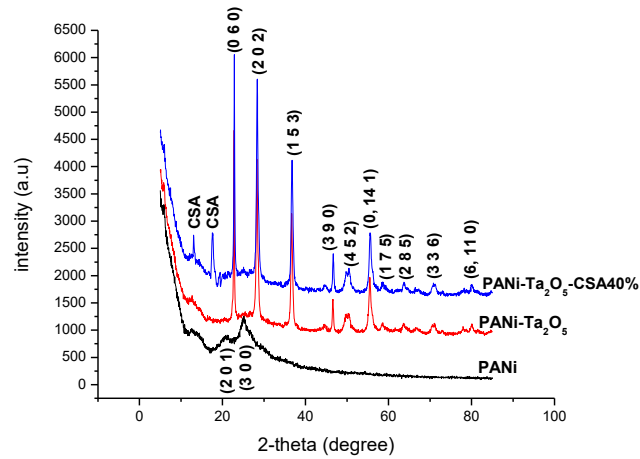


Fig. 2.21. XRD graphs of PANi-Ta<sub>2</sub>O<sub>5</sub>-CSA40% [75].

The peak at  $2\theta=20.68^\circ$  of PANi may be due to the periodicity developed parallel to the polymer chain and that at  $2\theta=25.24^\circ$  to the periodicity developed perpendicular to the polymer chain [57]. This ensures the formation of PANi in semi-crystalline form with the existence of both ordered and unordered regions. The peak at  $2\theta=25.24^\circ$  found to be more intense, narrow and well-defined. This signifies the presence of PANi in its conducting state (PANi-ES).

The XRD pattern of PANi-Ta<sub>2</sub>O<sub>5</sub> ensures the presence of Ta<sub>2</sub>O<sub>5</sub> in the nanocomposite. It is confirmed from the XRD graph that the crystal structure of Ta<sub>2</sub>O<sub>5</sub> remained intact even being dispersed in the PANi matrix.

The XRD pattern of PANi-Ta<sub>2</sub>O<sub>5</sub>-CSA40% reveals two distinct peaks at  $2\theta=13.04^\circ$  and  $2\theta=17.58^\circ$ . These two peaks clearly belong to CSA present in the crystal structure. The peaks at  $2\theta=50.43^\circ$  (452) and  $2\theta=55.38^\circ$  (0, 14 1) showed displacement which indicates change in the lattice structure of the nanocomposite upon addition of CSA. The other peaks of PANi-Ta<sub>2</sub>O<sub>5</sub>-CSA40% showed greater intensity with respect to those of PANi-Ta<sub>2</sub>O<sub>5</sub>. It can be remarked that PANi-Ta<sub>2</sub>O<sub>5</sub>-CSA40% possessed better crystallinity over PANi-Ta<sub>2</sub>O<sub>5</sub>.

The crystallite size of PANi has been calculated using Scherrer equation,  $D = k\lambda/\beta \cos\theta$ , where  $k$  is the particle shape factor (taken as 0.9),  $\lambda$  is the wavelength of Cu K $\alpha$  radiation ( $\lambda = 0.154$  nm),  $\theta$  is the diffraction angle and  $\beta$  is the full width at half maximum (FWHM) of the most prominent diffraction peak. The calculated average crystallite size of PANi found to be 6.3 nm. With addition of Ta<sub>2</sub>O<sub>5</sub>, the crystallite size of the nanocomposite increased to 12.49 nm. For the CSA doped nanocomposite, the crystallite size remained almost same as that of PANi- Ta<sub>2</sub>O<sub>5</sub>. This can be inferred that the crystalline behavior of PANi-Ta<sub>2</sub>O<sub>5</sub> and PANi-Ta<sub>2</sub>O<sub>5</sub>-CSA40% remained same. The addition of CSA does not have an effect on the crystallinity of the nanocomposite, but it may enhance the properties of the conducting polymer as suggested by higher intensity of the diffraction peaks [75].

Orthorhombic crystal system was selected for PANi-Ta<sub>2</sub>O<sub>5</sub> and PANi-Ta<sub>2</sub>O<sub>5</sub>-CSA40% on the basis of minimum deviation between inter-planar spacing of observed value and calculated value, and these are indexed accordingly. The lattice parameters are recorded as  $a=8.01311\text{\AA}$ ,  $b=26.9015\text{\AA}$  and  $c=4.9661\text{\AA}$ .

The crystallite size of pure PANi has been obtained using Scherrer equation,  $D = k\lambda/\beta \cos\theta$ , where  $k$  is the particle shape factor (taken as 0.9),  $\lambda$  is the wavelength of Cu K $\alpha$  radiation ( $\lambda = 0.154$  nm),  $\theta$  is the diffraction angle and  $\beta$  is the full width at half maximum (FWHM) of the highest and the most prominent diffraction peak. The calculated average crystallite size of PANi estimated as 6.3 nm. Upon addition of Ta<sub>2</sub>O<sub>5</sub>, the crystallite size of the nanocomposite increased to 12.49 nm. For the CSA doped nanocomposite, the crystallite size remained almost same as that of PANi-Ta<sub>2</sub>O<sub>5</sub>. It can be stated that the crystalline aspects of PANi-Ta<sub>2</sub>O<sub>5</sub> and PANi-Ta<sub>2</sub>O<sub>5</sub>-CSA40% remained alike. The addition of CSA does not have an impact on the crystallinity of the nanocomposite, but it may improve the properties of the conducting polymer as indicated by higher intensity of the diffraction peaks.

As can be seen from the XRD graphs, there is increase in crystallinity and hence better periodicity in the lattice for both PANi-Ta<sub>2</sub>O<sub>5</sub> and PANi-Ta<sub>2</sub>O<sub>5</sub>-CSA40% over pristine PANi. This may influence in better conductivity of the nanocomposite. Enhanced crystallinity of PANi-Ta<sub>2</sub>O<sub>5</sub>-CSA40% is also confirmed by SAED results as shown in Fig. 2.20.b. An increase in conductivity due to increase in crystallinity may be ascribed to two primary reasons – i) due to the difference in the intrinsic conductivity of the constituent materials of the composite and ii) alteration of the inter-particle spacing of the conductive fillers of the

resultant material [16]. The ordered arrangement of the crystalline region facilitates more smooth charge transfer than the unordered amorphous region.

#### 2.5.4 UV-Vis Spectroscopy analysis

The UV-Vis spectra of pure PANi and PANi-Ta<sub>2</sub>O<sub>5</sub>-CSA nanocomposites are shown in Fig.2.22. The spectra exhibited similar shape and each revealed one prominent broad peak centered within the range of 380 nm to 425 nm. This peak results from  $\pi$  to  $\pi^*$  transition of the benzenoid ring of PANi and excitation of the amine segment of the PANi chain [96].

The peak of pure PANi was observed at 412 nm. On the addition of Ta<sub>2</sub>O<sub>5</sub>, the spectral peak further broadened and slightly shifted towards a longer wavelength of 422 nm. This can be due to the change in the chemical structure of the PANi molecular structure upon its interaction with Ta<sub>2</sub>O<sub>5</sub>. The resultant molecule did not return to the original initial state, but jumped to a new ground state showing a different absorption spectrum. After doping with CSA, the peak of PANi-Ta<sub>2</sub>O<sub>5</sub>-CSA20% sample exhibited a significant shift towards higher frequency (blue shifting) at 410 nm. The peak of PANi-Ta<sub>2</sub>O<sub>5</sub>-CSA30% slightly moved to 415 nm, whereas for PANi-Ta<sub>2</sub>O<sub>5</sub>-CSA40%, the peak significantly displaced to 383 nm.

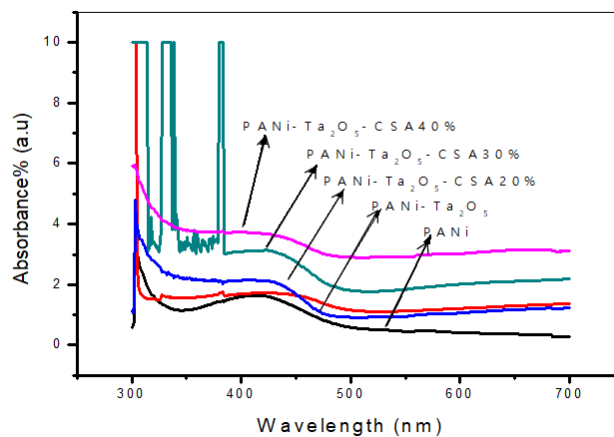


Fig. 2.22. UV-Vis Spectra of PANi, PANi-Ta<sub>2</sub>O<sub>5</sub> and PANi-Ta<sub>2</sub>O<sub>5</sub>-CSA samples [75].

The blue shifting may be caused due to increased oxidation state in the sample and hence better conductivity [113]. Thus, it is seen that the absorption peaks of PANi nanocomposites showing displacement towards longer wavelength confirm interaction with Ta<sub>2</sub>O<sub>5</sub> and the

doping effect of CSA. This results in further elongation of PANi conjugation chain and hence higher conductivity. This can further be explained that with the enhanced conjugation of the pi-system, the energy requirement for a  $\pi$  to  $\pi^*$  transition becomes increasingly less, and accordingly the wavelength of light absorbed becomes longer. Less energy is required to promote electrons from the ground state to the excited state. Thus the UV-Vis spectra of the CSA doped nanocomposites ensured greater length in their conjugation chain and can have better gas sensing attributes.

### 2.5.5 FTIR Spectroscopy analysis

The FTIR curves of pure PANi, PANi-Ta<sub>2</sub>O<sub>5</sub> and PANi-Ta<sub>2</sub>O<sub>5</sub>-CSA20% are shown in Fig. 2.23.a. The characteristic bands of PANi appeared at 729 cm<sup>-1</sup> (C–C, C–H bonding mode of aromatic ring), 936 cm<sup>-1</sup> (C–H out of plane bonding in benzenoid ring), 1441 cm<sup>-1</sup> (C–N stretching of benzenoid ring) and 1553.40 cm<sup>-1</sup> (C–N stretching of quinoid ring). Thus, these characteristic peaks confirm the formation of PANi.

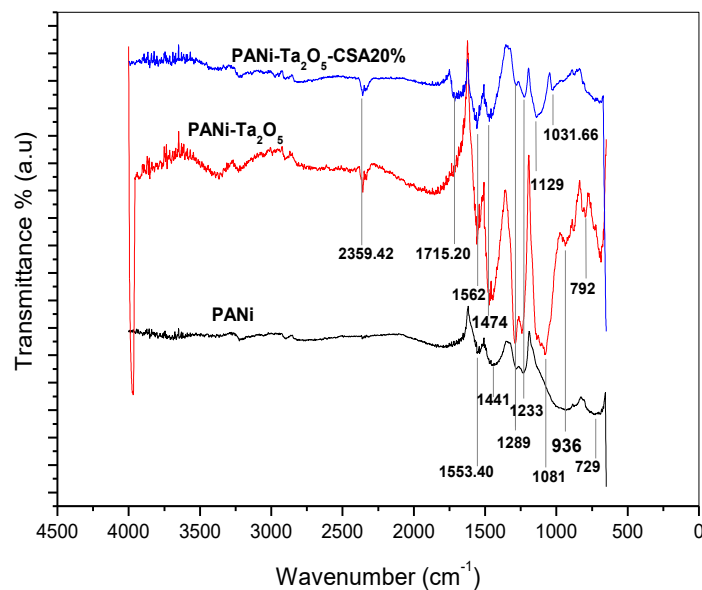


Fig. 2.23.a. FTIR spectra of PANi, PANi- Ta<sub>2</sub>O<sub>5</sub> and PANi- Ta<sub>2</sub>O<sub>5</sub>-CSA20% [75].

The spectrum of PANi-Ta<sub>2</sub>O<sub>5</sub> nanocomposite exhibited two prominent peaks at 792 cm<sup>-1</sup> and 1081 cm<sup>-1</sup>. These may be caused by the stretching vibration mode of O=Ta=O bonds. The peaks at 1227 cm<sup>-1</sup> and 1289 cm<sup>-1</sup> belong to PANi-Ta<sub>2</sub>O<sub>5</sub> molecule. The fresh peak at 2359.42 cm<sup>-1</sup> can be ascribed to the stretching vibrations of Ta=O bonds. The spectrum, also, reveals some blue shifts relative to that of pure PANi. These include 1553.40–1562.18 cm<sup>-1</sup>

and 1441–1474  $\text{cm}^{-1}$ . On addition of  $\text{Ta}_2\text{O}_5$  into the pure PANi matrix, the original peaks have been shifted to higher frequencies due to increased overall molecular mass and interaction with  $\text{Ta}_2\text{O}_5$ . This can be remarked that  $\text{Ta}_2\text{O}_5$  is attached to the polymer chain through a kind of Van Der Waals force [44].

The addition of 20 wt% CSA into PANi- $\text{Ta}_2\text{O}_5$  caused the formation of new peaks at 1031.66  $\text{cm}^{-1}$ , 1129  $\text{cm}^{-1}$  and 1715.20  $\text{cm}^{-1}$ . This resulted due to the =S=O bond for CSA.

Fig. 2.23.b illustrates the FTIR spectra of 30% and 40% CSA doped nanocomposites and they are analyzed to study the effect of increasing percentage of CSA into the PANi molecule. Some important peak displacements can be noticed such as 592-624  $\text{cm}^{-1}$  and 1122.42-1138.91  $\text{cm}^{-1}$ . Comparing the spectra of 20% and 30% doped CSA samples, shifts such as 1031.66-807  $\text{cm}^{-1}$ , 1129-1122.42  $\text{cm}^{-1}$  and 1233-1304  $\text{cm}^{-1}$  can be observed. These blue or red shifts ensure the increasing doping levels of CSA within the PANi nanocomposite.

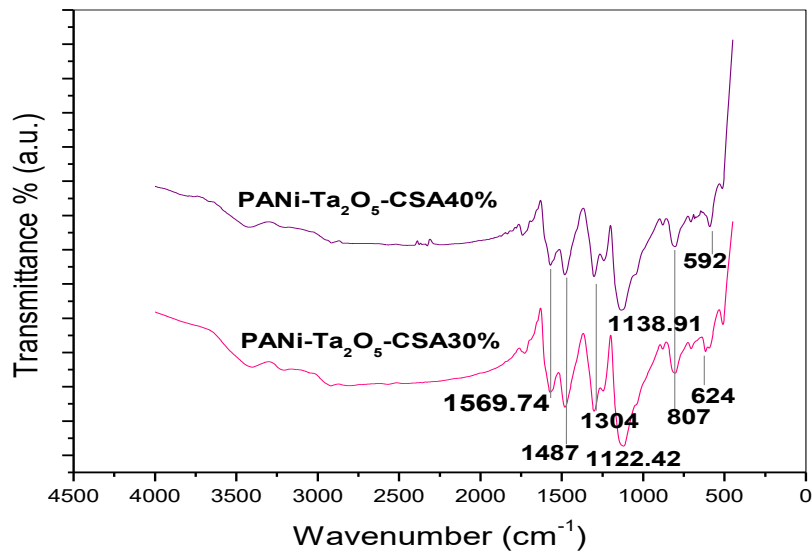


Fig.2.23.b. FTIR spectra of PANi- $\text{Ta}_2\text{O}_5$ -CSA30% and PANi-  $\text{Ta}_2\text{O}_5$ -CSA40% [75].

Table- 2.3

(FTIR analysis of PANi, PANi-Ta<sub>2</sub>O<sub>5</sub> and CSA doped PANi-Ta<sub>2</sub>O<sub>5</sub>)

Wavenumber cm <sup>-1</sup>	Characteristic Peak
2359.42	Stretching vibration mode due to Ta=O for Ta <sub>2</sub> O <sub>5</sub>
1553.40	C-N stretching of quinoid Rings
1441	C-N stretching of benzenoid ring
1233	C-N stretching of benzenoid ring
1129	= S = O for CSA
1081	Stretching vibration mode due to O=Ta=O for Ta <sub>2</sub> O <sub>5</sub>
936	C-H out of plane bonding in benzenoid ring
729	C-C, C-H bonding mode of aromatic ring

## 2.6. Chapter conclusions

This chapter detailed the preparation of pure PANi in emeraldine salt and base form, and PANi-Ta<sub>2</sub>O<sub>5</sub> nanocomposites doped with 20%, 30% and 40% of CSA respectively using chemical oxidative polymerization process. The samples obtained in fine powdered form were characterized by SEM, TEM, XRD, UV-Vis and FTIR spectroscopic techniques. SEM results exhibited highly agglomerated globular structures of the CSA doped PANi-Ta<sub>2</sub>O<sub>5</sub> nanocomposite posing it as a suitable candidate for gas sensing. XRD plots demonstrate high crystallinity of the PANi-Ta<sub>2</sub>O<sub>5</sub>-CSA40% nanocomposite. This can result in improved conductivity of the sensing material.

The  $\pi$  to  $\pi^*$  transitions of the benzenoid ring were noticed in the UV-Vis spectra. This can attribute to better conjugation of the polymer chain. The FTIR spectra ensure the chemical structure of the samples and confirm the formation of the nanocomposites.

\*\*\*\*\*